

THE HOT GAS CONTENT OF LOW-LUMINOSITY EARLY-TYPE GALAXIES AND THE IMPLICATIONS REGARDING SUPERNOVA HEATING AND AGN FEEDBACK

LAURENCE P. DAVID, CHRISTINE JONES, WILLIAM FORMAN, IRIS MONICA VARGAS & PAUL NULSEN
Harvard-Smithsonian Center for Astrophysics, 60 Garden St., Cambridge, MA 02138;
david@head.cfa.harvard.edu
accepted for publication by the The Astrophysical Journal

ABSTRACT

We have analyzed Chandra observations of 18 low-luminosity early-type galaxies with $L_B \lesssim 3 \times 10^{10} L_{\odot B}$. Thermal emission from hot gas with temperatures between 0.2 and 0.8 keV comprises 5-70% of the total 0.5-2.0 keV emission from these galaxies. We find that the total X-ray luminosity from LMXBs (resolved plus the power-law component of the unresolved emission) scales roughly linearly with the K-band luminosity of the galaxies with a normalization comparable to that found in more luminous early-type galaxies. All of the galaxies in our sample are gas poor with gas masses much less than that expected from the accumulation of stellar mass loss over the life time of the galaxies. The average ratio of gas mass to stellar mass in our sample is $M_{gas}/M_* = 0.001$, compared to more luminous early-type galaxies which typically have $M_{gas}/M_* = 0.01$. The time required to accumulate the observed gas mass from stellar mass loss in these galaxies is typically 3×10^8 yr. Since the cooling time of the gas is longer than the replenishment time, the gas cannot be condensing out of the hot phase and forming stars, implying that the gas is most likely being expelled from these galaxies in a wind. The one exception to this is NGC4552, which is the most optically luminous galaxy in our sample and has the highest gas content. Using recent estimates of the Type Ia supernova rate and AGN heating rate in early-type galaxies, we find that, on average, heating by Type Ia supernovae should exceed AGN heating in galaxies with $L_B \lesssim 3 \times 10^{10} L_{\odot B}$. We also find that heating by Type Ia supernovae is energetically sufficient to drive winds in these galaxies, even if the present Type Ia supernova rate is overestimated by a factor of two or the present stellar mass loss rate is underestimated by a factor of two. There is significant scatter in the gas properties of galaxies with comparable optical luminosities. Nearly continuous heating by Type Ia supernovae alone cannot account for the large scatter in observed gas mass. We suggest that the scatter in gas properties could arise from periodic AGN outbursts, during which time AGN heating dominates over Type Ia supernova heating, or environmental factors, such as a high pressure environment which would suppress the formation of strong galactic winds.

Subject headings: galaxies:elliptical and lenticular – galaxies:ISM – X-ray:binaries – X-ray:galaxies – X-ray:ISM

1. INTRODUCTION

Heating by supernovae and active galactic nuclei (AGN) are thought to play important roles in galaxy formation, generating the observed correlation between the bulge mass of a galaxy and the mass of the central supermassive black hole, the upper mass cutoff of galaxies and reheating the gas in galaxies, groups and clusters. In order to reconcile the predictions of the cold dark matter hierarchical clustering scenario with the observed luminosity function of galaxies and their mass-to-light ratios, it is thought that supernova feedback regulates star formation in galaxies less luminous than about $3 \times 10^{10} L_{\odot B}$, while AGN feedback regulates star formation in more massive galaxies (e.g., White & Frank 1991; Bower et al. 2005; Croton et al. 2006). Only Type II supernovae provide a natural feedback mechanism due to the short time delay between the onset of star formation and the first supernova. While Type Ia supernovae (SN Ia) cannot provide a feedback mechanism that regulates concurrent star formation, SN Ia can play a significant role in the fate of gas shed by evolving stars in low-mass galaxies long after star formation ceases.

Einstein observations showed that the bulk of the X-ray emission from optically luminous early-type galaxies arises from hot gas in hydrostatic equilibrium (Forman, Jones & Tucker 1985). A harder X-ray component, more prevalent among low-luminosity early-type galaxies, was detected by ASCA and assumed to arise from low-mass X-ray binaries (LMXBs) due to

the old stellar population in these systems (Kim, Fabbiano & Trinchieri 1992). Based on the analysis of ASCA data, White, Sarazin & Kulkarni (2002) found that the luminosity of the hard X-ray component was more strongly correlated with the luminosity in globular clusters rather than the total optical luminosity of the galaxies. Chandra, with its superior angular resolution, has resolved populations of point sources in many early-type galaxies (e.g., Sarazin, Irwin & Bregman 2000; Angelini, Lowenstein & Mushotzky 2001; Kraft et al. 2001; Blanton, Sarazin & Irwin 2001) and found that 20 to 80% of the point sources reside in globular clusters (Sarazin et al. 2003).

While the hot gas content of X-ray luminous early-type galaxies has been well studied by Chandra and previous X-ray telescopes, little is known about the properties of the gas in less luminous early-type galaxies. In low-luminosity early-type galaxies, the X-ray emission from LMXBs can exceed the thermal emission from hot gas, so it is imperative that the LMXBs be detected and excised from the analysis of the diffuse emission. Theoretical models concerning the evolution of early-type galaxies show that for typical SN Ia rates, early-type galaxies fainter than $M_B \approx -20$ should possess SN Ia driven galactic winds (e.g., David, Forman & Jones 1990, 1991). In addition to heating by SN Ia, AGN heating may also expel a significant portion of the gas shed by evolving stars in the shallow potential well of low-luminosity galaxies. Chandra has detected X-ray cavities filled with radio emitting plasma and AGN driven shocks in many elliptical galaxies and clusters (e.g., McNamara

TABLE 1
LOW-LUMINOSITY EARLY-TYPE GALAXY SAMPLE

Name	D_L (Mpc)	M_B	Type	L_K ($L_{\odot,K}$)	σ_* (km s^{-1})	ObsIds	Exposure (ksec)
ESO 0428-G014	24.3	-19.96	-1.6	3.62×10^{10}	-	4866	28.1
NGC 821	24.1	-20.19	-5.0	8.79×10^{10}	199.0	4006 4408	22.9
NGC 1023	11.4	-20.21	-3.0	8.44×10^{10}	204.0	4696	10.5
NGC 1386	16.5	-18.97	-0.6	3.47×10^{10}	166.0	4076	19.6
NGC 1389	21.7	-19.24	-3.3	3.91×10^{10}	132.0	4169	38.4
NGC 2434	21.6	-20.10	-5.0	7.38×10^{10}	205.0	2923	19.2
NGC 2787	7.48	-17.76	-1.0	1.46×10^{10}	194.0	4689	31.4
NGC 3115	9.68	-20.19	-3.0	8.95×10^{10}	266.0	2040	34.6
NGC 3245	20.9	-19.95	-2.0	5.92×10^{10}	220.0	2926	9.6
NGC 3377	11.2	-19.18	-5.0	2.75×10^{10}	131.0	2934	38.7
NGC 3379	10.6	-19.94	-5.0	7.31×10^{10}	201.0	1587	31.2
NGC 3608	22.9	-20.11	-5.0	5.24×10^{10}	204.0	2073	38.1
NGC 4251	19.6	-20.03	-2.0	6.67×10^{10}	119.0	4695	10.5
NGC 4435	11.4	-18.68	-2.0	2.38×10^{10}	157.0	2883	24.6
NGC 4459	16.1	-19.83	-1.0	7.58×10^{10}	172.0	2927	9.5
NGC 4552	15.3	-20.36	-5.0	1.05×10^{11}	261.0	2072	53.3
NGC 4697	11.7	-20.28	-5.0	9.12×10^{10}	165.0	4727 4728	72.6
NGC 5866	15.3	-20.10	-1.0	9.04×10^{10}	159.0	2879	28.0

Notes: Galaxy name, luminosity distance (D_L), absolute blue magnitude (M_B), Galaxy Type in RC3, K-band luminosity (L_K) based on $M_{K\odot} = 3.33$ within the the same aperture as that used to extract the X-ray spectrum, stellar velocity dispersion (σ_*), Chandra ObsIds used in the analysis, and the cleaned ACIS exposure time.

et al. 2000, Finoguenov & Jones 2002, Fabian et al. 2003, Blanton et al. 2003, Nulsen et al. 2005a, Nulsen et al. 2005b; Forman et al. 2005). Based on the analysis of cavities found in a sample of galaxies, groups and clusters, Birzan et al. (2004) determined that the mechanical power of AGNs can be up to 10^4 times their radio power. Thus, the thermal and dynamic properties of the hot gas in low-luminosity early-type galaxies are sensitive probes of the present SN Ia rate and AGN activity in these galaxies.

This paper is organized in the following manner. In § 2, we present our low-luminosity early-type galaxy sample. Section 3 contains the details of our Chandra data reduction. The spectroscopic results for the LMXBs and diffuse emission are discussed in § 4 and the observed scaling between the total X-ray luminosity of the LMXB population and the K-band luminosity of the galaxies is presented in § 5. Sections 6 and 7 discuss the properties of the hot gas, the inferred characteristics of the galactic winds, and the implications regarding the Fe abundance in galaxies with galactic winds. In § 8, we examine the relative importance of AGN and SN Ia heating in these galaxies. Possible origins of the large scatter in the observed gas properties among the galaxies are discussed in § 9 and the main results of our paper are summarized in § 10.

2. GALAXY SAMPLE

Jones et al. (2006) have compiled a sample of early-type galaxies that have been observed by the Chandra X-ray observatory. We initially extracted a sample of galaxies with M_B between -18 and -20.4 (corresponding to L_B between 3×10^9 and $3 \times 10^{10} L_{\odot,B}$). Galaxies with near-by companions and total ACIS exposure times less than 5 ksec were then excluded from our sample. After a preliminary analysis of the Chandra data,

we also excluded galaxies with fewer than 100 total net counts from further analysis. Our final sample of 18 low-luminosity early-type galaxies is shown in Table 1 along with their optical and infrared properties and cleaned ACIS exposure times. The absolute blue magnitudes given in Table 1 are computed from $m_B(T^0)$ (RC3; de Vaucouleurs et al. 1991) and the distance moduli given in Tonry et al. (2001) if available. Otherwise, we use the corrected redshift in Faber et al. (1989), or finally, the uncorrected redshifts. We use $H_0=70 \text{ km s}^{-1} \text{ Mpc}^{-1}$ throughout. The K-band apparent magnitudes and luminosities given in Table 1 are derived directly from the 2MASS K-band images and are computed within the same aperture used to extract the X-ray spectrum from the galaxy. The stellar velocity dispersion is obtained from Faber et al. (1989), if available, otherwise we use the average stellar velocity dispersion from the literature as given in the LEDA catalog.

3. DATA REDUCTION

All *Chandra* archival observations of the galaxies in our sample were reprocessed with CIAO 3.2.2 and CALDB 3.1.0 and screened for background flares. Fifteen of the galaxies in our sample were imaged on the S3 chip, two on the I3 chip and one on the S2 chip. Multiple exposures of the same galaxy were combined into a single exposure. For each galaxy, we generated a 0.3-6.0 keV image at full spatial resolution for the chip on which the target was imaged. We then ran the CIAO *wavdetect* tool on each 0.3-6.0 keV image with a detection threshold of 10^{-6} to generate the point source regions. Unlike more luminous early-type galaxies, the galaxies in our sample have little hot gas, so the point source detection efficiency is fairly uniform across the galaxies. There is some area on the ACIS chip

TABLE 2
SPECTRAL ANALYSIS OF COMBINED EMISSION FROM NON-NUCLEAR POINT SOURCES

Name	N	N_{bg}	$L_{X,min}$ (erg s ⁻¹)	$N_H(gal)$ (10 ²⁰ cm ⁻²)	Γ	χ^2/DOF	$F_{X,res}$ (erg s ⁻¹ cm ⁻²)	$L_{X,res}$ (erg s ⁻¹)
ESO 0428-G014	3	0.26	7.2×10^{37}	22.2	1.6	-	4.19×10^{-15}	2.7×10^{38}
NGC 821	6	0.38	1.2×10^{38}	6.24	1.6	-	1.20×10^{-14}	7.8×10^{38}
NGC 1023	13	2.2	5.6×10^{37}	7.06	1.40 (1.06-1.74)	4.2/5	4.32×10^{-14}	5.6×10^{38}
NGC 1386	7	0.59	5.0×10^{37}	1.41	1.6	-	2.18×10^{-14}	6.5×10^{38}
NGC 1389	6	0.22	1.4×10^{38}	1.47	1.65 (1.33-1.99)	9.7/8	3.02×10^{-14}	1.6×10^{39}
NGC 2434	11	0.29	7.0×10^{37}	12.2	1.44 (1.12-1.77)	4.0/5	2.83×10^{-14}	1.5×10^{39}
NGC 2787	17	1.8	6.7×10^{36}	4.39	1.26 (1.09-1.43)	16.5/15	3.74×10^{-14}	2.2×10^{38}
NGC 3115	52	2.9	9.2×10^{36}	4.61	1.46 (1.40-1.52)	70.0/66	1.45×10^{-13}	1.5×10^{39}
NGC 3245	3	0.36	1.4×10^{38}	2.11	1.6	-	1.39×10^{-14}	6.4×10^{38}
NGC 3377	25	3.1	1.1×10^{37}	2.77	1.35 (1.26-1.45)	49.4/37	6.35×10^{-14}	8.4×10^{38}
NGC 3379	42	4.6	1.0×10^{37}	2.79	1.66 (1.61-1.72)	93.1/75	1.81×10^{-13}	2.2×10^{39}
NGC 3608	18	1.0	7.5×10^{37}	1.48	1.38 (1.08-1.70)	2.3/6	2.10×10^{-14}	1.2×10^{39}
NGC 4251	7	0.14	2.0×10^{38}	1.85	1.6	-	2.35×10^{-14}	1.1×10^{39}
NGC 4435	6	0.03	3.5×10^{37}	2.61	1.75 (1.41-2.11)	6.6/5	2.25×10^{-14}	3.5×10^{38}
NGC 4459	5	0.55	9.0×10^{37}	2.68	1.6	-	1.34×10^{-14}	3.7×10^{38}
NGC 4552	89	5.0	1.8×10^{37}	2.56	1.36 (1.32-1.40)	160/128	1.87×10^{-13}	4.9×10^{39}
NGC 4697	79	8.2	7.4×10^{36}	2.14	1.52 (1.48-1.57)	130/122	1.42×10^{-13}	2.1×10^{39}
NGC 5866	29	1.3	2.9×10^{37}	1.47	1.75 (1.62-1.89)	19.2/21	5.79×10^{-14}	1.5×10^{39}

Notes: Galaxy name, number of detected non-nuclear point sources (N), expected number of background sources (N_{bg}), luminosity of a source in the galaxy with a flux equal to the 3σ point source detection limit ($L_{X,min}$), galactic hydrogen column density ($N_H(gal)$), best-fit power-law index (Γ) and 90% confidence limit, χ^2 per degrees of freedom, and the background subtracted (both the diffuse and AGN components of the X-ray background) 0.5-2.0 keV flux ($F_{X,res}$) and luminosity ($L_{X,res}$) of the combined emission from the detected non-nuclear point sources. The flux and luminosity for spectra with fewer than 100 counts were calculated assuming $\Gamma = 1.6$ and galactic absorption.

beyond the D_{25} optical isophote for all the galaxies in our sample so we can obtain a local background. This is essential for the detection of 0.3-0.8 keV gas, since the X-ray background below 0.8 keV is subject to galactic emission and charge exchange emission from solar wind particles in the Earth's magnetosphere (Wargelin et al. 2004). There is also a spatial gradient in the depth of the contaminant on the ACIS filters which affects the spectral shape of the background below 1 keV. We therefore exclude data in the bottom and top 200 rows on ACIS-S and beyond a $5'$ radius from the center of ACIS-I from further analysis. Observations of the ACIS external calibration source show that the depth of the contaminant is fairly uniform in the remaining regions¹. Our screening procedure ensures an accurate subtraction of the soft X-ray background which is vital for determining the gas properties in these galaxies.

4. SPECTRAL ANALYSIS

Using the point source regions generated by *wavdetect* along with the D_{25} optical isophote, we extracted three spectra for each galaxy: 1) a spectrum containing the combined emission from all detected non-nuclear point sources within the D_{25} isophote, 2) a spectrum of the unresolved emission within D_{25} (i.e., the emission outside of the detected source regions), and 3) a background spectrum from the unresolved emission beyond the D_{25} isophote. A point source is identified as an AGN if it is located within $2.0''$ of the centroid of the galaxy as determined from the 2MASS K-band image. None of our galaxies

has more than one point source within this region. The spectra for the detected sources and the unresolved emission were binned to a minimum of 20 counts per bin and corresponding photon weighted response and area files were generated using the CIAO tasks *mkacisrmf* and *mkwarf*.

4.1. Point Source Population

The background subtracted (i.e., the unresolved component of the X-ray background) spectra of the combined emission from the detected non-nuclear point sources with more than 100 net counts were fitted to an absorbed power-law model with the absorption fixed at the galactic value. Our analysis shows that the emission from the binary populations is well fitted by a power-law spectrum with $\Gamma \approx 1.6$ (see Table 2). This result is consistent with the spectral analysis of the combined emission from LMXBs in a sample of 15 early-type galaxies analyzed by Irwin, Athey & Bregman (2003). In cases where the combined emission from the detected point sources results in fewer than 100 net counts, the fluxes are derived assuming galactic absorption and $\Gamma = 1.6$. To estimate the number of background point sources and integrated flux, we used the 0.5-2.0 keV luminosity function derived from the Chandra Deep Field-South (Rosati et al. 2002) and the 3σ point source detection threshold in each observation. The total number of detected non-nuclear point sources and the expected number of background AGN above the 3σ detection limit are shown in Table 2. The resulting background subtracted (both unresolved and AGN) 0.5-2.0 keV flux

¹ <http://cxc.harvard.edu/ciao/why/acisqedeg.html>

TABLE 3
RESULTS OF FITTING THE DIFFUSE EMISSION TO AN ABSORBED POWER-LAW

Name	Γ	χ^2/DOF
ESO 0428-G014	2.8 (2.0-3.6)	11.9/10
NGC 821	1.7 (1.0-2.4)	17.6/19
NGC 1023	2.5 (2.0-3.0)	13.2/13
NGC 1386	3.0 (2.8-3.2)	111/45
NGC 1389	1.8 (1.1-2.6)	15.7/14
NGC 2434	2.8 (2.6-3.0)	125/38
NGC 2787	2.6 (2.3-2.8)	20.1/13
NGC 3115	1.9 (1.8-2.0)	43.4/29
NGC 3245	3.0 (2.7-3.3)	19.6/12
NGC 3377	2.5 (2.2-2.8)	15.9/15
NGC 3379	2.0 (1.8-2.2)	39.4/32
NGC 3608	3.4 (3.2-3.6)	41.0/14
NGC 4251	2.0 (1.5-2.4)	5.6/8
NGC 4435	3.0 (2.7-3.2)	39.5/38
NGC 4459	1.9 (1.6-2.3)	50.4/13
NGC 4552	2.3 (2.1-2.4)	4062/133
NGC 4697	2.8 (2.7-2.9)	344/84
NGC 5866	2.6 (2.5-2.7)	183/67

Notes: Galaxy name, best-fit power-law index (Γ) and 90% confidence limit, and the χ^2 per degrees of freedom.

and luminosity for the combined point source emission in each galaxy are given in Table 2. Due to the small angular extent of the galaxies, variations in the number of background AGN do not have a significant effect on the derived fluxes. There are also very few photons from the diffuse background component within the source regions. The primary uncertainty in the derived X-ray flux is the uncertainty in the spectral model. For Γ between 1.2 and 2.0, the estimated 0.5-2.0 keV flux varies by 25%.

4.2. Diffuse Emission

The unresolved diffuse emission in each observation must contain some emission from LMXBs with fluxes below the point source detection limit. The low gas temperature ($kT \approx 0.3 - 0.6$ keV) in these galaxies makes it easier to separate the thermal and power-law components compared to more X-ray luminous early-type galaxies which typically have gas temperatures around 1 keV. We first fit the diffuse emission with an absorbed power-law model. Except for N1389, N821 and N4251, the best fit index is significantly steeper than that obtained from fitting the combined emission from the detected point sources (see Table 3), indicating the presence of a diffuse soft component. We then fit the diffuse spectra with an absorbed power-law plus MEKAL model with the absorption frozen at the galactic value and the abundance of heavy elements frozen at the solar value (see the results in Table 4). In all but three cases (N1389, N821 and N4251), adding a thermal component improved the fit at greater than the 95% confidence level based on a F-test. The resulting best-fit power-law indices in the two component model are consistent with those derived from fitting the combined emission from the detected point sources. This shows that the spectral index of LMXBs does not vary significant with luminosity, which is consistent with Chandra observations of the lowest luminosity LMXBs in our Galaxy (Wilson et al. 2003). For N1389, N821 and N4251, we determined the 90% upper limit on the thermal flux

by increasing the normalization of the MEKAL model until the resulting χ^2 increased by 2.71 compared to the best-fit with a pure power-law model.

Besides emission from hot gas, there are other potential sources for the unresolved soft X-ray emission, including: supersoft sources, M stars and RS CVn systems. Pellegrini & Fabbiano (1994) showed that both K-M main-sequence stars, due to the reduced rotation rate in old stars, and Rs CVn systems are unlikely to produce a significant component of the soft X-ray emission in early-type galaxies. Supersoft sources are characterized by black body emission with $kT < 100$ eV. Supersoft sources are probably a combination of several types of objects, including: postnovae hot white dwarf, symbiotics, pre-white dwarfs in planetary nebulae, accreting white dwarfs and possibly accreting intermediate mass black holes (Kahabka & van den Heuvel 1997). A scatter plot of gas temperature vs. stellar velocity dispersion for our galaxy sample is shown in Fig. 1. The solid line in Fig. 1 is the relation found by O’Sullivan, Ponman & Collins (2003) for a sample of more X-ray luminous early-type galaxies with typical velocity dispersions between 250 and 350 km s⁻¹. While there is significant scatter in Fig. 1, the relation between gas temperature and velocity dispersion in our sample of galaxies is in reasonable agreement with that observed in hotter systems providing strong evidence that the soft X-ray emission in our sample arises from hot gas. Gas shed by evolving stars thermalizes at the temperature associated with the stellar velocity dispersion of the stars ($T_* = \mu m_p \sigma_*^2/k$), which is shown as a dashed line in Fig. 1. The ratio of energy per unit mass in the stars to that in the gas, $\beta_{spec} = T_*/T_{gas}$, varies from 0.3 to 1 in our sample, which is comparable to values found in more X-ray luminous early-type galaxies, giving further support to a gaseous origin for the soft unresolved emission.

TABLE 4
RESULTS OF FITTING THE DIFFUSE EMISSION TO AN ABSORBED POWER-LAW PLUS MEKAL MODEL

Name	Γ	kT (keV)	χ^2 /DOF	$L_{X,unres}$ (erg s ⁻¹)	$L_{X,LMXB}$ (erg s ⁻¹)	f_{unres} (%)	$L_{X,gas}$ (erg s ⁻¹)	f_{gas} (%)
ESO 0428-G014	0.8 (0.4-2.0)	0.60 (0.34-0.83)	5.9/8	2.5×10^{38}	5.2×10^{38}	48	9.5×10^{38}	65
NGC 821	1.7	0.4	14.6/17	1.1×10^{39}	1.9×10^{39}	58	$< 7.0 \times 10^{38}$	< 27
NGC 1023	2.5 (1.2-3.5)	0.78 (0.34-1.10)	6.2/11	4.6×10^{38}	1.0×10^{39}	46	5.3×10^{38}	35
NGC 1386	1.7 (0.6-2.7)	0.29 (0.25-0.32)	68.0/43	8.1×10^{38}	1.5×10^{39}	54	2.4×10^{39}	61
NGC 1389	1.8	0.4	14.7/12	4.9×10^{38}	2.1×10^{39}	23	$< 5.7 \times 10^{38}$	< 21
NGC 2434	1.9 (1.4-2.5)	0.51 (0.44-0.58)	26.8/36	1.4×10^{39}	3.0×10^{39}	47	6.0×10^{39}	67
NGC 2787	2.0 (0.8-3.1)	0.35 (0.27-0.60)	6.1/11	1.8×10^{38}	4.0×10^{38}	45	2.1×10^{38}	34
NGC 3115	1.6 (1.4-1.7)	0.52 (0.36-0.74)	23.7/28	5.5×10^{38}	2.0×10^{39}	27	3.2×10^{38}	14
NGC 3245	2.4 (1.4-3.8)	0.32 (0.22-0.54)	11.5/10	7.8×10^{38}	1.4×10^{39}	56	1.1×10^{39}	44
NGC 3377	1.9 (0.9-2.7)	0.21 (0.12-0.38)	10.6/13	2.0×10^{38}	1.0×10^{39}	20	1.6×10^{38}	14
NGC 3379	1.9 (1.5-2.4)	0.65 (0.20-1.1)	34.8/30	6.6×10^{38}	2.8×10^{39}	24	1.2×10^{38}	4
NGC 3608	2.4 (1.9-3.1)	0.35 (0.29-0.47)	19.2/12	1.4×10^{39}	2.6×10^{39}	54	2.7×10^{39}	51
NGC 4251	2.0	0.4	4.9/6	9.2×10^{38}	2.0×10^{39}	46	$< 7.8 \times 10^{38}$	< 28
NGC 4435	2.4 (1.5-4.0)	0.39 (0.28-0.85)	28.7/36	5.2×10^{38}	8.7×10^{38}	60	4.8×10^{38}	36
NGC 4459	0.9 (0.4-1.7)	0.42 (0.32-0.52)	18.4/11	4.0×10^{38}	7.7×10^{38}	52	1.8×10^{39}	70
NGC 4552	1.9 (1.8-2.0)	0.54 (0.51-0.56)	179/131	3.4×10^{39}	8.3×10^{39}	41	1.8×10^{40}	68
NGC 4697	1.6 (1.0-2.2)	0.33 (0.31-0.36)	92.2/81	1.8×10^{38}	2.3×10^{39}	8	2.1×10^{39}	47
NGC 5866	1.1 (0.9-1.2)	0.32 (0.30-0.35)	84.3/65	6.2×10^{38}	2.1×10^{39}	29	2.2×10^{39}	51

Notes: Galaxy name, best-fit power-law index (Γ) and temperature (kT) along with their 90% confidence limits, χ^2 per degrees of freedom, X-ray luminosity of the power-law component of the diffuse emission ($L_{X,unres}$), total X-ray luminosity of the LMXBs ($L_{X,LMXB} = L_{X,res} + L_{X,unres}$), fraction of the power-law component that is unresolved (f_{unres}), X-ray luminosity of the thermal component of the diffuse emission ($L_{X,gas}$), and the fraction of the total luminosity arising from gas (f_{gas}). All luminosities are given in the 0.5-2.0 keV bandpass. The values of $L_{X,gas}$ and f_{gas} for NGC821, NGC1389, and NGC4251 correspond to 90% upper limits.

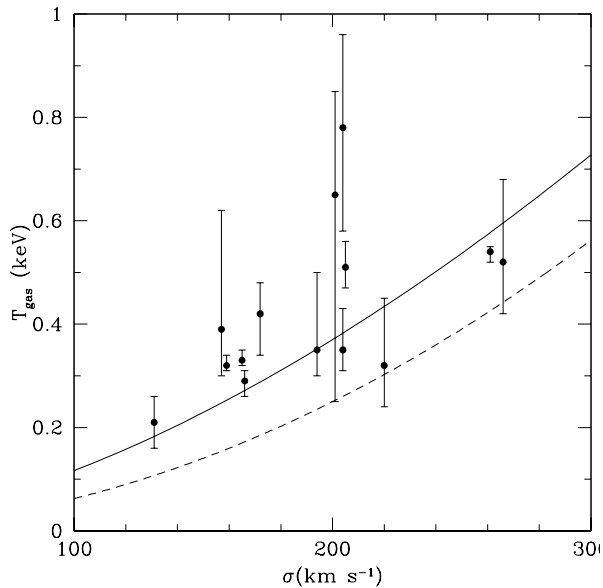


FIG. 1.— Scatter plot of the best-fit temperature of the diffuse emission vs. the stellar velocity dispersion. The solid line is the relation between T_{gas} and σ_* found by O'Sullivan et al. (2003) for a sample of more X-ray luminous early-type galaxies and the dashed line is the temperature associated with the stellar velocity dispersion in the galaxies.

We also can use the Chandra data directly to place limits on the contribution to the diffuse emission from supersoft sources. Chandra has detected supersoft sources in many galaxies (Sarazin, Irwin & Bregman 2000; Pence et al. 2001; Swartz

et al. 2002; Di Stefano & Kong 2004) and there appears to be a general trend that supersoft sources are more common in the spiral arms of late-type galaxies compared to bulge dominated systems. Sarazin et al. (2000) identified 3 supersoft sources in NGC 4697 based on hardness ratios. Di Stefano & Kong (2004) fitted the combined emission from the 3 supersoft sources in NGC 4697 to an absorbed black body model and obtained a temperature of $kT = 80$ eV and a 0.3-7.0 keV flux of 1.89×10^{-14} erg cm⁻² s⁻¹. Based on this spectral model, and converting between bandpasses, this gives a 0.5-2.0 keV flux of 6.0×10^{-15} erg cm⁻² s⁻¹, which is only 2% of the total resolved 0.5-2.0 keV flux of NGC4697 given in Table 2. Adding an 80 eV black body component in the spectral analysis of the diffuse emission does not significantly improve the fit in any of the galaxies in our sample. For NGC 4697, the 90% upper limit on the 0.5-2.0 keV flux of an 80 eV black body component is 6.0×10^{-15} erg cm⁻² s⁻¹, which is twice the flux of the resolved supersoft sources, but only 4% of the flux in the thermal component of the unresolved emission.

5. SCALING BETWEEN $L_{X,lmxb}$ AND THE K-BAND LUMINOSITY

Earlier studies based on *Einstein* and *ROSAT* observations showed that $L_x \propto L_B^2$ for early-type galaxies more luminous than $L_B \approx 3 \times 10^{10} L_\odot$ and $L_x \propto L_B$ for less luminous galaxies (Forman, Jones & Tucker 1985; Trinchieri & Fabbiano 1985; O'Sullivan, Forbes & Ponman 1991). The different slopes were thought to arise from the competition between the two primary

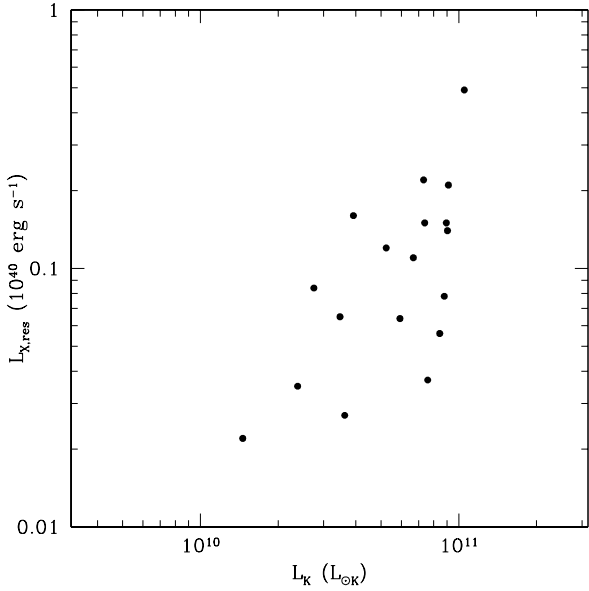


FIG. 2.— Scatter plot of the combined 0.5-2.0 keV luminosity of the resolved LMXBs vs. the K-band luminosity of the galaxies.

sources of X-rays in early-type galaxies, with emission from LMXBs dominating in low luminosity galaxies and thermal emission from hot gas dominating in more luminous galaxies. Observations of early-type galaxies by Chandra are able to study these two components separately. With the availability of 2MASS data, it is more appropriate to use L_K instead of L_B since it is a better proxy for stellar mass. The combined 0.5-2.0 keV luminosity of only the resolved LMXBs is plotted against the K-band luminosity of the galaxies in Fig. 2 and the total 0.5-2.0 keV luminosity of the LMXBs ($L_{LMXB} = L_{X,res} + L_{X,unres}$) is plotted against the K-band luminosity of the galaxies in Fig. 3. Due to the range in sensitivity among the observations (see Table 2), there is significant scatter in Fig. 2. By combining the power-law component of the unresolved emission with the resolved LMXB emission, the scatter is significantly reduced in Fig. 3 and there is an overall linear trend between L_{LMXB} and L_K . The most X-ray luminous galaxy in Figs. 2 and 3 is NGC4552, which is discussed more extensively in §9. Fitting a power-law to the data in Fig. 3 yields a best-fit of:

$$L_{LMXB} = 3.7 \times 10^{38} \left(\frac{L_K}{10^{10} L_{\odot K}} \right)^{0.81} \text{ erg s}^{-1} \quad (1)$$

which is shown as a solid line in Fig. 3. Several studies have shown that the spatial distribution of LMXBs follows the light in early-type galaxies (Sarazin et al. 2001; Gilfanov 2002; Jordan et al. 2004), so our estimate of L_{LMXB}/L_K should be valid within any aperture.

Both Colbert et al. (2004) and Kim & Fabbiano (2004) estimated the ratio of L_{LMXB} to L_K for samples of more X-ray luminous early-type galaxies. In these studies, L_{LMXB} was computed in the 0.3-8.0 keV bandpass assuming a count rate conversion factor appropriate for power-law spectra with $\Gamma = 1.7 - 1.8$ and galactic absorption. The difference between the spectral index used in our work and these studies does not make a significance difference on the derived luminosities. However, their 0.3-8.0 keV luminosities should be 3 times our 0.5-2.0 keV luminosities. Both studies only included the emission from

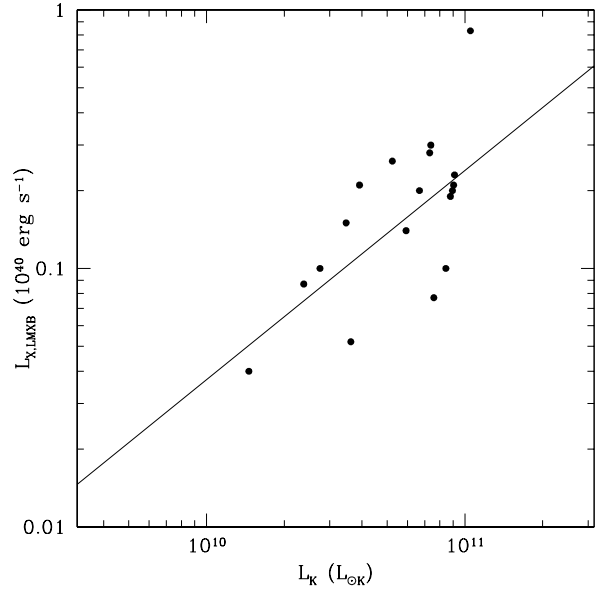


FIG. 3.— Scatter plot of the total 0.5-2.0 keV luminosity of the LMXBs (resolved plus the power-law component of the unresolved emission) vs. the K-band luminosity of the galaxies.

non-nuclear point sources within the D_{25} isophote. Kim & Fabbiano computed L_{LMXB} by integrating over the galaxy's LMXB luminosity function. Colbert et al. derived a relation of $L_{LMXB} = 1.3 \times 10^{-4} L_K$, where $L_K = \nu L_{\nu}$. From the 2MASS documentation², $\nu F_{\nu}(m_K = 0) = 9.27 \times 10^{-7} \text{ erg cm}^{-2} \text{ s}^{-1}$. Rewriting their expression in terms of $L_{\odot K}$, and adjusting for bandpass differences, gives a coefficient in eq. (1) of $2.3 \times 10^{38} \text{ erg s}^{-1}$, which is 50% lower than our estimate. After correcting for bandpass differences, the ratio of L_{LMXB} to L_K in Kim & Fabbiano is a factor of 1.8 higher than our result. Thus, within a factor of two, we find the same ratio of L_{LMXB} to L_K in our sample of low-luminosity early-type galaxies as that found in more X-ray luminous systems.

Previous studies have suggested that $L_{X,LMXB}$ is better correlated with the total luminosity in globular clusters (White, Sarazin & Kulkarni 2002) and that the dispersion in the $L_{X,LMXB}-L_K$ relation is correlated with the specific frequency of globular clusters, S_N (Kim & Fabbiano 2004). A search of the literature only uncovered published values of S_N for half of the galaxies in our sample, and most of these estimates have large errors, so we cannot investigate the dependence of $L_{X,LMXB}$ on S_N in our sample.

6. THE HOT GAS CONTENT

There is significant scatter in $L_{X,gas}$ compared to $L_{X,LMXB}$ with a factor of 100 variation in $L_{X,gas}$ for a given L_K (see Fig. 4). The ratio of $L_{X,gas}$ to $L_{X,LMXB}$ also shows significant scatter and varies from 0.04 to 2.2 (see Fig. 5). We also divided the sample into ellipticals ($T < -3$) and S0s ($T > -3.0$). The average $L_{X,gas}$ is essentially the same for ellipticals and S0s, but the ellipticals have a greater dispersion (see Fig. 4). Early-type galaxies can be classified as "core" or "cuspy" depending on their inner stellar surface brightness profile. Based on ROSAT observations, Pellegrini (2005) found that for a given optical luminosity, core early-type galaxies are more X-ray luminous

² <http://www.ipac.caltech.edu/2mass>

TABLE 5
 HOT GAS CONTENT

Name	R_m (kpc)	$n_{e,0}$ (cm^{-3})	M_{gas} (M_\odot)	\dot{M}_* ($M_\odot \text{ yr}^{-1}$)	t_g (yr)	t_c (yr)
ESO 0428-G014	4.8	9.5×10^{-3}	2.0×10^7	0.065	3.1×10^8	2.2×10^9
NGC 821	7.0	$< 1.3 \times 10^{-2}$	$< 5.0 \times 10^7$	0.158	$< 3.2 \times 10^8$	-
NGC 1023	6.9	5.6×10^{-3}	2.2×10^7	0.152	1.4×10^8	5.4×10^9
NGC 1386	5.7	1.8×10^{-2}	4.9×10^7	0.062	7.9×10^8	7.0×10^8
NGC 1389	5.7	$< 1.4 \times 10^{-2}$	$< 3.9 \times 10^7$	0.070	$< 5.5 \times 10^8$	-
NGC 2434	7.5	2.1×10^{-2}	9.3×10^7	0.133	7.0×10^8	1.4×10^9
NGC 2787	3.9	5.6×10^{-3}	8.2×10^6	0.026	3.1×10^8	1.6×10^9
NGC 3115	5.8	5.5×10^{-3}	1.6×10^7	0.161	9.9×10^7	4.6×10^9
NGC 3245	7.3	1.1×10^{-2}	4.6×10^7	0.107	4.3×10^8	1.6×10^9
NGC 3377	6.5	4.7×10^{-3}	1.7×10^7	0.049	3.5×10^8	2.6×10^9
NGC 3379	7.7	3.1×10^{-3}	1.4×10^7	0.132	1.1×10^8	1.3×10^{10}
NGC 3608	9.3	1.4×10^{-2}	9.0×10^7	0.094	9.6×10^8	1.4×10^9
NGC 4251	6.8	$< 8.4 \times 10^{-3}$	$< 3.2 \times 10^7$	0.120	$< 2.7 \times 10^8$	-
NGC 4435	4.0	7.7×10^{-3}	1.2×10^7	0.043	2.8×10^8	1.4×10^9
NGC 4459	7.0	1.2×10^{-2}	4.7×10^7	0.136	3.4×10^8	1.6×10^9
NGC 4552	10.7	3.2×10^{-2}	2.5×10^8	0.189	1.3×10^9	1.3×10^9
NGC 4697	9.1	1.3×10^{-2}	8.2×10^7	0.164	5.0×10^8	1.5×10^9
NGC 5866	6.7	1.6×10^{-2}	5.9×10^7	0.163	3.6×10^8	1.0×10^9

Notes: Galaxy name, the radius of a circular aperture which has the same area as the region used to extract the diffuse X-ray spectrum (R_m), central electron number density ($n_{e,0}$), gas mass (M_{gas}) within R_m , stellar mass loss rate (\dot{M}_*) estimated from L_K in Table 1, the time to accumulate the observed gas mass given the present stellar mass loss rate (t_g), and the average radiative cooling time of the gas (t_c).

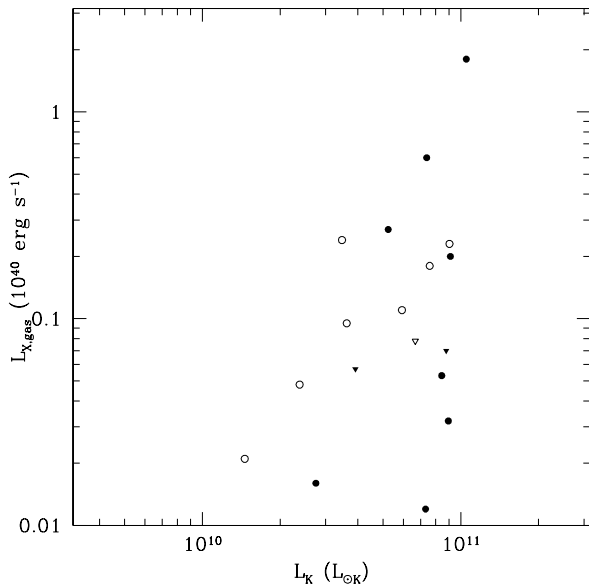


FIG. 4.— Scatter plot of the 0.5-2.0 keV luminosity of the thermal component of the diffuse emission ($L_{X, gas}$) vs. the K-band luminosity of the galaxies. Triangles correspond to 90% upper limits. Filled symbols represent ellipticals ($T < -3$) and open symbols represent lenticulars ($T > -3$).

than cuspy galaxies. We searched the literature for HST derived stellar surface brightness profiles of the galaxies in our sample, but only found results for 8 galaxies, so we cannot draw any general conclusions. However, the galaxies with the highest $L_{X, gas}$ (NGC4552) and lowest $L_{X, gas}$ (NGC3379) in our sample both have flat cores (Lauer et al. 2005). There is a

fairly strong correlation between $L_{X, gas}$ and kT among X-ray luminous early-type galaxies (O’Sullivan, Ponman & Collins 2003). Our sample of lower luminosity galaxies, however, does not show such a correlation (see Fig. 6), suggesting that non-gravitational heating mechanisms have a more significant impact on the gas properties of lower luminosity galaxies.

The gas density and mass can be estimated from the emission measure of the best-fit MEKAL model to the diffuse emission along with an assumption about the spatial distribution of the gas. The soft photon statistics in the Chandra data are insufficient to permit an empirical determination of the surface brightness profile of each galaxy. Past studies have shown that the X-ray surface brightness of luminous early-type galaxies is well fitted with a β model with $\beta \approx 0.5$ and a core radius between 1 and 3 kpc (Forman, Jones & Tucker 1985). David, Forman & Jones (1990, 1991) generated a grid of elliptical galaxy models with different kinematic states of the hot gas (e.g., cooling flows, partial winds, total subsonic winds, and total transonic winds) and found that the surface brightness profile of these models could be characterized with β between 0.3 and 0.5. Table 5 contains the derived central gas density and mass in each galaxy assuming $\beta = 0.5$ and a core radius of 1 kpc. This calculation also assumes that the diffuse emission arises from within a circular region centered on the galaxy with a radius of R_m (given in Table 5) which has the same area as that in the region used to extract the X-ray spectrum of the diffuse emission. Varying β between 0.3 and 0.67 or the core radius between 1 and 10 kpc only changes the estimated gas mass by 40%.

All of the early-type galaxies in our sample are gas poor with an average $M_{gas} \approx 3 \times 10^7 M_\odot$ (see Table 5). Based on stellar

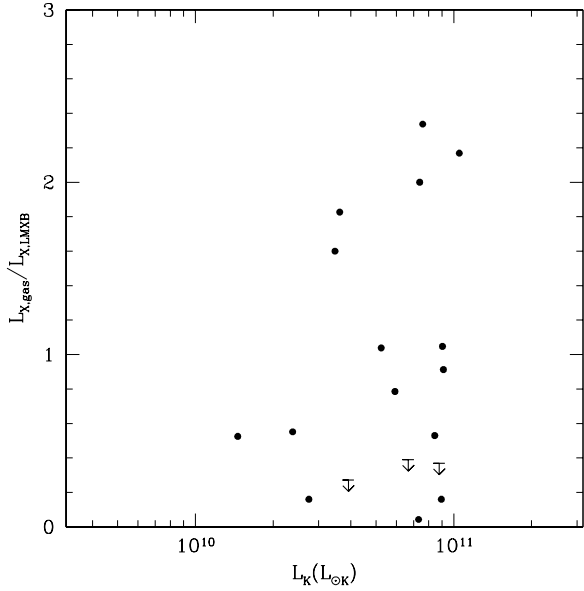


FIG. 5.— Ratio of the gas luminosity to total LMXB luminosity vs. the K-band luminosity.

evolution models of early-type galaxies, Bell & de Jong (2001) derived an expression of $\log(M_*/L_K) = -0.692 + 0.652(B - V)$, where M_* is the stellar mass. The mean B-V in our sample is 0.9, which gives $M_*/L_K = 0.8M_\odot/L_{\odot K}$ (consistent with dynamical measurements of a sample of early-type galaxies by Humphrey et al. 2006) and $M_{gas}/M_* = 8.0 \times 10^{-4}$. A cumulative histogram of M_{gas}/M_* for our sample is shown in Fig. 7. For comparison, Fukazawa et al. (2006) recently analyzed Chandra observations of 53 X-ray luminous early-type galaxies and found average values of $n_{e,0} = 0.1 \text{ cm}^{-3}$, $M_{gas} = 3 \times 10^9 M_\odot$ and $M_{gas}/M_* = 0.01$. Fig. 8 shows that there is significant scatter in M_{gas}/M_* for a given L_K among the galaxies in our sample, but even the most gas rich system in our sample (NGC4552) does not have as high a gas content as the mean value in the Fukazawa et al. sample.

For a Salpeter initial mass function, stars shed approximately 30% of their initial mass over a Hubble time, which gives an average ejected mass of $2 \times 10^{10} M_\odot$ per galaxy in our sample. Very little of this gas can accrete into the central supermassive black hole. Based on the average stellar velocity dispersion in our sample ($\sigma_* = 200 \text{ km s}^{-1}$) and the observed correlation between the central black hole mass and σ_* (Gebhardt et al. 2000), the average M_{bh} in our sample should be approximately $1.2 \times 10^8 M_\odot$. To determine how long it takes to accumulate the observed gas mass, we use a present day stellar mass loss rate from asymptotic giant branch stars of $\dot{M}_* = 0.078(L_B/10^{10} L_{\odot B}) M_\odot \text{ yr}^{-1}$, which is consistent with the derived stellar mass loss rate from a sample of 9 ellipticals observed by the *Infrared Space Observatory* (Athey et al. 2002). Converting this stellar mass loss rate to the K-band and using L_K within the same aperture used to extract the diffuse spectrum (see Table 1), we find that the time to accumulate the derived gas mass in these galaxies is $t_g \approx 1 - 3 \times 10^8 \text{ yr}$ (see Table 5). The typical cooling time of the gas ($t_c = 5kTM_{gas}/(2\mu m_p L_{bol})$) shown in Table 5 is $t_c \approx 10^9 \text{ yr}$. Since the cooling time is longer than the replenishment time, the gas cannot be condensing out of the hot phase and forming stars. Thus, most of the gas shed by evolving stars must have been expelled from these galaxies in a wind. The only exception to this is NGC4552 (M89),

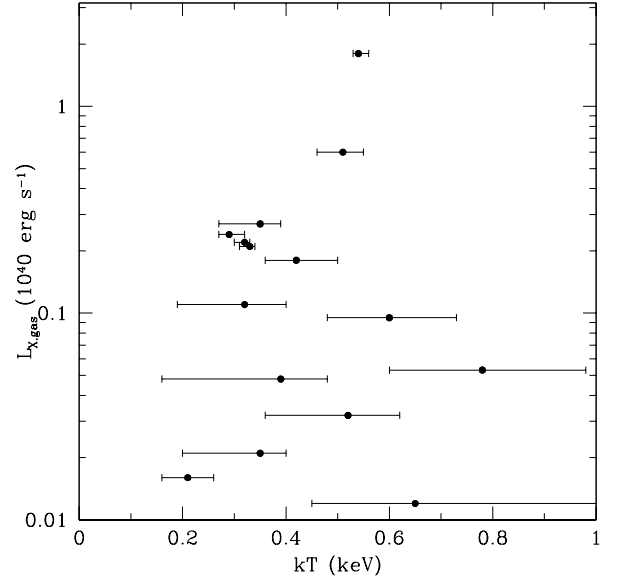


FIG. 6.— Scatter plot of the 0.5-2.0 keV luminosity of the thermal component of the diffuse emission ($L_{X,gas}$) against the best-fit temperature. The errors bars on the temperature are shown at the 1σ confidence level.

which is the most optically luminous galaxy in our sample, has the highest gas content, and is located in the densest environment. The Chandra image of NGC4552 shows that it has a significant gaseous corona and that it is presently being ram pressure stripped of its gas as it falls into the Virgo cluster (Machacek et al. 2005).

There have been many theoretical studies regarding the dynamical evolution of the hot gas in early-type galaxies (e.g., Mathews & Baker 1971; Loewenstein & Mathews 1987; David, Forman & Jones 1990, 1991; Ciotti et al. 1991; Pellegrini & Fabbiano 1994; Brighenti & Mathews 1999). The primary quantity that determines the present dynamic state of the gas is the ratio of the mass averaged temperature of the stellar ejecta to the depth of the gravitational potential well of the galaxy. The mass averaged temperature of stellar ejecta is given by $T_* = \dot{M}_{SNIa} T_{SNIa} / \dot{M}_*$, where $T_{SNIa} = 2\mu m_p E_{SNIa} / (3kM_{ej})$ and $\dot{M}_{SNIa} = M_{ej} v_{SNIa}$. Using $E_{SNIa} = 10^{51} \text{ erg}$ and $M_{ej} = 1.4M_\odot$, gives $T_{SNIa} = 150 \text{ keV}$ per particle. A large grid of models have been generated over the past 20 years covering a range of galaxy masses, SN Ia rates, stellar initial mass functions and mass-to-light ratios. Most models have used SN Ia rates between 1/4 and one times Tamman's (1982) rate of $v_{SNIa} = 0.88h^2 \text{ SNU}$ (where h is the Hubble constant in units of $100 \text{ km s}^{-1} \text{ Mpc}^{-1}$ and a SNU = $1/100 \text{ yr} / 10^{10} L_{\odot B}$) and a stellar mass loss rate of approximately $\dot{M}_* = 0.15(L_B/10^{10} L_{\odot B}) M_\odot \text{ yr}^{-1}$ (Faber & Gallagher 1976). Converting to $H_0 = 70 \text{ km s}^{-1} \text{ Mpc}^{-1}$, these rates give $T_* = 1.5 - 6.0 \text{ keV}$ per particle. Using the more recent estimate of \dot{M}_* from Athey et al. (2002) and $v_{SNIa} = 0.16 \text{ SNU}$ (for $H_0 = 70 \text{ km s}^{-1} \text{ Mpc}^{-1}$) from Cappellaro et al. (1999), gives $T_* = 4.2 \text{ keV}$ per particle. In the appendix, we show that the minimum energy required to remove the gas shed by stars in a wind is equal to the mass averaged binding energy of the injected gas (eq. 19). We computed this minimum energy in detail for NGC1023, which has a stellar velocity dispersion close to the mean in our sample, assuming a Navarro, Frenk & White (1996) distribution with a concentration parameter of 10 for the

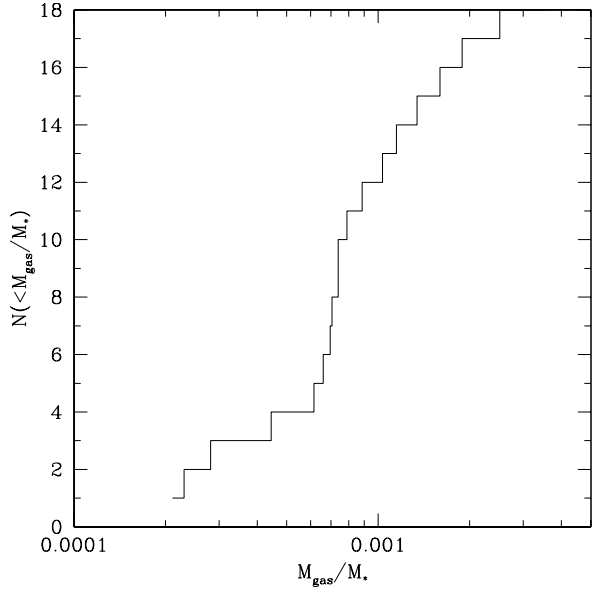


FIG. 7.— Cumulative histogram of M_{gas}/M_* .

dark matter and a King model for the stellar distribution with a core radius of $51.9''$ (Jarrett et al. 2003). This calculation gives a minimum energy of 2.01 keV per particle, which is equal to $7.2\sigma_*^2$ in NGC1023.

If the gas is in a steady-state wind, then $\dot{M}_* = 4\pi R_m^2 \rho_{\text{gas}}(R_m) u_w(R_m)$, where $\rho_{\text{gas}}(R_m)$ is the gas density at R_m , which can be estimated from the central gas density and the assumed β model, and $u_w(R_m)$ is the bulk gas velocity at R_m . Using the stellar mass loss rates and central gas densities in Table 5 give $u_w \lesssim 35 \text{ km s}^{-1}$ (see Table 6). The mechanical power of the winds ($\dot{E}_w = \dot{M}_* u_w^2 / 2$) is a small fraction of the expected energy injection rate from SN Ia ($\dot{E}_{\text{SN Ia}}$) (see Table 6). As shown in Fig. 1, the gas in these galaxies requires an additional heating of approximately 0.3 keV per particle above purely gravitational heating, which is only 5% of the expected SN Ia heating rate. Supernova explosions in low-luminosity early-type galaxies should not experience significant radiative losses due to the lack of cold gas and the long cooling time of the hot gas. Thus, most of the SN Ia supernova energy must be used in lifting the gas out of the gravitational potential well of the galaxies. Based on our detailed calculation for NGC1023 presented above, the rate of increase in the total gravitational binding energy of the gas due to stellar mass loss can be estimated as $\dot{W} = 7.2 \dot{M}_* \sigma_*^2$. Table 6 shows that $\dot{E}_{\text{SN Ia}}$ is 2-6 times \dot{W} for the galaxies in our sample based on the recent stellar mass loss rate in Athey et al. (2002) and the SN Ia rate in Cappellaro et al. (1999), indicating that the energy released by SN Ia is sufficient to drive galactic winds in these galaxies. Using the Faber & Jackson relation (1976), $\dot{E}_{\text{SN Ia}}/\dot{W} \propto L_K^{-1/2}$, indicating that heating by Type Ia supernovae is less efficient in driving the gas out of more luminous galaxies, which accounts for the higher gas content in these systems.

NGC 4552 is the only galaxy in our sample without a galactic wind. NGC4552 and NGC3115 have the lowest ratios of $\dot{E}_{\text{SN Ia}}$ to \dot{W} in our sample with values of 2.0 and 1.9 (see Table 7). Given the uncertainties in $\dot{E}_{\text{SN Ia}}$ and \dot{W} , it is possible that SN Ia are energetically incapable of driving a wind in NGC4552. While NGC4552 has the highest gas content in our sample, it is still less than that found in more luminous early-type galaxies.

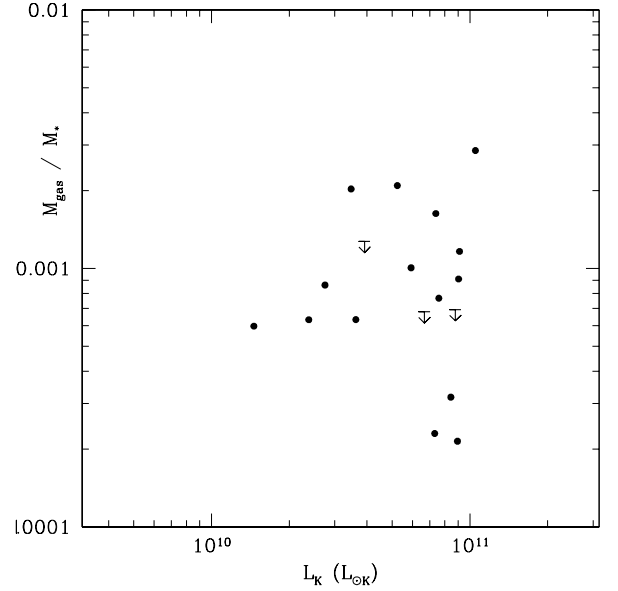


FIG. 8.— Scatter plot of the ratio of gas mass to stellar mass (M_{gas}/M_*) vs. the K-band luminosity of the galaxies.

The Chandra image shows that the low gas content in NGC4552 is due to ram pressure stripping of its gas as it falls into the Virgo cluster. Another possible explanation for the lack of a recent wind and the build-up of a gaseous corona in NGC4552 is that the ambient gas pressure in the Virgo cluster was sufficient to suppress the formation of a galactic wind before NGC4552 experienced significant ram pressure stripping. This would explain the low gas content of the more isolated galaxy NGC3115 (which was able to develop a galactic wind due to the lack of a confining ambient medium) compared to NGC4552, even though they have very similar ratios of $\dot{E}_{\text{SN Ia}}$ to \dot{W} .

7. IMPLICATIONS FOR THE FE ABUNDANCE OF THE HOT GAS

The gas in these low luminosity galaxies should have an iron abundance equal to the mass averaged abundance of the stellar and SN Ia ejecta. Based on our adopted rates given above, the gas should have an abundance 10 times the solar value in Grevesse & Suval (1998) assuming that each SN Ia generates $0.7M_{\odot}$ of Fe. The primary difficulty in determining the gas density and abundance (primarily Fe) of the hot gas in these galaxies is the difficulty in measuring the thermal continuum when there is residual emission from unresolved LMXBs in the diffuse emission. Fig. 9 shows the best-fit absorbed power-law plus MEKAL model (assuming solar abundances) to the diffuse emission in NGC1386, where 45% of the total LMXBs emission is unresolved. Notice that the power-law emission exceeds the thermal continuum at all energies. There is a strong degeneracy between the emission measure and abundance in the fitting process. For example, freezing the abundance at 10 times the solar value and refitting the spectrum simply reduces the flux in the thermal continuum by a factor of 10, while keeping the flux in the Fe-L lines and the power-law component essentially the same. Freezing the normalization and index of the power-law model does not reduce the degeneracy. The temperature determination is robust, since it is derived from the centroid of the blended Fe-L lines. Since the emission measure is proportional to $n_e n_H$ and the flux in the Fe-L lines is proportional to $n_e n_{\text{Fe}}$, it is difficult to accurately determine the gas mass and Fe abundance in these galaxies due to the emission

TABLE 6
HOT GAS ENERGETICS

Name	u_w (km s ⁻¹)	\dot{E}_w (erg s ⁻¹)	\dot{E}_{SNIa} (erg s ⁻¹)	\dot{W} (erg s ⁻¹)	\dot{E}_w/\dot{W}
ESO 0428-G014	8.9	1.6×10^{36}	4.3×10^{40}	-	-
NGC 821	-	-	1.0×10^{41}	2.9×10^{40}	3.4
NGC 1023	29	4.0×10^{37}	1.0×10^{41}	2.8×10^{40}	3.6
NGC 1386	4.2	3.5×10^{35}	4.1×10^{40}	7.8×10^{39}	5.2
NGC 1389	-	-	4.6×10^{40}	5.6×10^{39}	8.2
NGC 2434	6.4	1.8×10^{36}	8.7×10^{40}	2.4×10^{40}	3.6
NGC 2787	6.8	3.9×10^{35}	1.7×10^{40}	4.5×10^{39}	3.8
NGC 3115	35	6.2×10^{37}	1.0×10^{41}	5.2×10^{40}	1.9
NGC 3245	10	3.5×10^{36}	7.0×10^{40}	2.4×10^{40}	2.9
NGC 3377	11	2.0×10^{36}	3.2×10^{40}	3.8×10^{39}	8.4
NGC 3379	31	2.8×10^{37}	8.6×10^{40}	2.4×10^{40}	3.6
NGC 3608	6.0	1.1×10^{36}	6.2×10^{40}	1.7×10^{40}	3.6
NGC 4251	-	-	7.8×10^{40}	8.0×10^{39}	9.7
NGC 4435	8.1	9.0×10^{35}	2.8×10^{40}	4.9×10^{39}	5.7
NGC 4459	12	6.3×10^{36}	8.9×10^{40}	1.8×10^{40}	4.9
NGC 4552	4.7	1.3×10^{36}	1.2×10^{41}	5.9×10^{40}	2.0
NGC 4697	11	6.6×10^{36}	1.1×10^{41}	2.0×10^{40}	5.5
NGC 5866	11	6.4×10^{36}	1.1×10^{41}	1.9×10^{40}	5.8

Notes: Galaxy name, required wind velocity (u_w) to expel the gas from the galaxy at the same rate as the present stellar mass loss rate, mechanical energy of the wind (\dot{E}_w), SN Ia heating rate (\dot{E}_{SNIa}), the required heating rate to remove the stellar mass loss from the gravitational potential of the galaxy (\dot{W}) and the ratio \dot{E}_w/\dot{W} .

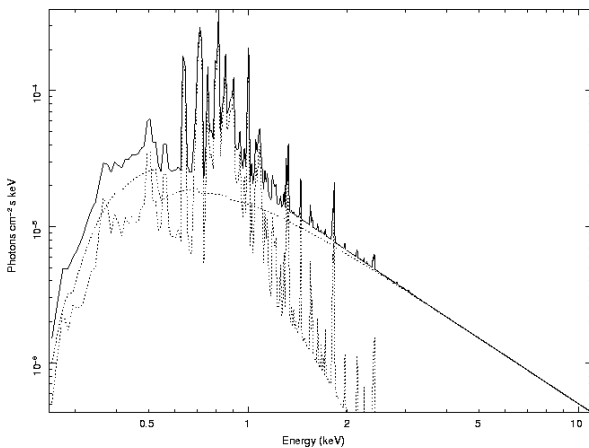


FIG. 9.— Best-fit absorbed power-law plus MEKAL model to the diffuse emission in N1386. The lower curve shows the thermal emission, the middle curve shows the power-law component, and the upper curve is the sum of the thermal plus power-law models.

from unresolved LMXBs. If the gas in these galaxies has an Fe abundance that is 10 times the solar value, then the central gas densities, gas masses, replenishment times and cooling times in Table 5 should be reduced by a factor of 3. In addition, the wind velocities in Table 6 should be increased by a factor of 3 and the mechanical power of the winds should be increased by an order of magnitude. Hence, a higher Fe abundance actually strength-

ens the argument for galactic winds due to the decrease in gas mass and increase in wind velocity. The conclusion that SN Ia are energetically capable of driving galactic winds in these galaxies is not affected by the Fe abundance of the gas, since this argument mainly depends on the present SN Ia rate, stellar mass loss rate and the stellar velocity dispersion in the galaxies.

8. IS AGN HEATING IMPORTANT?

Chandra has detected X-ray cavities and AGN driven shocks in several early-type galaxies (M84 - Finoguenov & Jones 2002; NGC4636 - Jones et al. 2002; Cen A - Kraft et al. 2003). The Chandra image of NGC4552 shows the presence of two spherical AGN driven shocks (Machacek et al. 2005). None of the other galaxies in our sample exhibit any substructure in the diffuse emission, but it is, of course, much easier to detect cavities and shocks in galaxies with significant amounts of hot gas. Seven of the galaxies in our sample were detected in the NVSS (Condon et al. 1998). The 1.4 GHz luminosity (νL_ν), or upper limit, for the galaxies is given in Table 7. Fig. 10 shows that there is no obvious trend between M_{gas}/M_* and νL_ν , however, there is a suggestion that the most radio luminous AGNs reside in galaxies with the highest gas content.

The radio luminosity of an AGN is a poor indicator of its mechanical power. Using Chandra observations of a sample of galaxies and clusters with X-ray cavities, Birzan et al. (2004) found that the ratio of mechanical to radio power varies from 10 in the most radio luminous AGNs, up to 10^4 in systems with less radio luminous AGNs. Based on these results and a survey of radio-loud galaxies, Best et al. (2006) derived a time-averaged mechanical AGN heating rate of $1.6 \times 10^{41} (M_{bh}/10^8 M_\odot)^{1.6} \text{ erg s}^{-1}$. Using the relation between black

TABLE 7
RADIO PROPERTIES OF CENTRAL AGN

Name	S_ν (mJy)	νL_ν (erg s $^{-1}$)
ESO 0428-G014	81.0	8.0×10^{37}
NGC 821	< 2.3	< 2.2×10^{36}
NGC 1023	< 2.3	< 5.0×10^{35}
NGC 1386	37.1	1.7×10^{37}
NGC 1389	< 2.3	< 1.8×10^{36}
NGC 2434	< 2.3	< 1.8×10^{36}
NGC 2787	10.9	1.0×10^{36}
NGC 3115	< 2.3	< 3.6×10^{35}
NGC 3245	6.7	4.9×10^{36}
NGC 3377	< 2.3	< 4.8×10^{35}
NGC 3379	2.4	4.5×10^{35}
NGC 3608	< 2.3	< 2.0×10^{36}
NGC 4251	< 2.3	< 1.5×10^{36}
NGC 4435	< 2.3	< 5.0×10^{35}
NGC 4459	< 2.3	< 9.9×10^{35}
NGC 4552	100.1	3.9×10^{37}
NGC 4697	< 2.3	< 5.2×10^{35}
NGC 5866	21.8	8.5×10^{36}

Notes: Galaxy name, 1.4 GHz flux (S_{mJy}) and luminosity (νL_ν) of the central AGN.

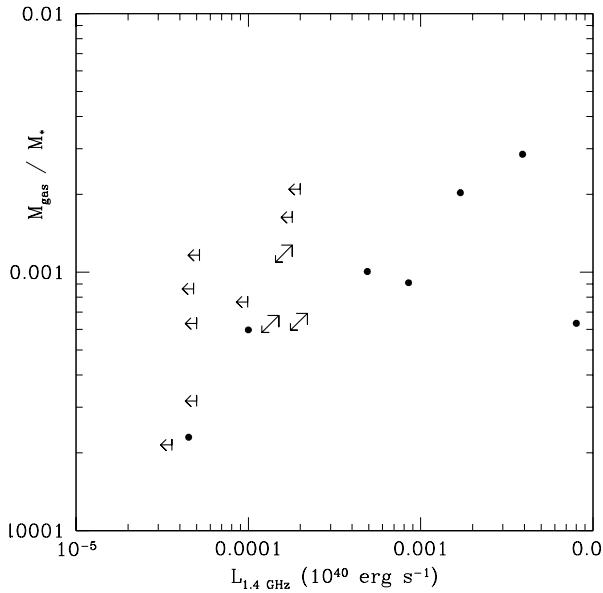


FIG. 10.— Scatter plot of the gas mass to stellar mass ratio (M_{gas}/M_*) vs. the 1.4 GHz radio luminosity of the central AGN. The leftward pointing arrows represent upper limits on the 1.4 GHz luminosity and the arrows pointing to the lower left represent upper limits on both the 1.4 GHz luminosity and gas mass.

hole mass and the absolute red magnitude, M_R , found by McLure & Dunlop (2002) of $\log(M_{bh}/M_\odot) = -0.50M_R - 2.96$, and an average $R - K$ of 2.5 for the galaxies in our sample, we plot the expected AGN and SN Ia heating rates in Fig. 11 against the bolometric luminosity of the hot gas. For comparison, the mechanical power required to generate the observed shocks in NGC4552 (the upper right hand point in Fig. 11) is 3×10^{41} erg s $^{-1}$ (Machacek et al. 2005), which is a factor of

2 greater than the rate predicted by Best et al. (2006), but certainly within the uncertainties. Fig. 11 indicates that heating by SN Ia should dominate the energetics of the gas in early-type galaxies with $L_K \lesssim 10^{11} L_{\odot K}$ and that AGN heating should dominate in more luminous galaxies.

9. DISCUSSION

If heating by SN Ia is the dominant mechanism for expelling the gas shed by evolving stars from low-luminosity early-type galaxies, it is a puzzle as to why there is so much scatter in M_{gas}/M_* and $L_{X,gas}$ (see Figs. 7 and 11) given that supernova heating is essentially a continuous process. Since the gas masses are computed in different apertures (see Table 5), we checked to see if there is a correlation between M_{gas}/M_* and aperture size and found none. While the time-averaged SN Ia heating rate shown in Fig. 11 exceeds the time-averaged AGN heating rate, except for possibly the most luminous galaxies in our sample, the episodic nature of AGN outbursts could produce times during which mechanical AGN heating exceeds SN Ia heating. Thus, the large observed scatter could be a reflection of recent AGN activity. The sound crossing time within the central 10 kpc in these galaxies is approximately 3×10^7 yr. If AGN outbursts repeat on a shorter time scale, then the gas will not be able to establish a steady-state wind. In the very center of the galaxies, heating by SN Ia cannot be thought of as a continuous process. For example, within an enclosed stellar mass of $10^6 M_\odot$, there will only be one SN Ia every 3.0×10^7 yr. During this time, the stars within this region will shed a total of $50 M_\odot$ of gas. If this gas is converted into mechanical energy by the central black hole with an efficiency of 10%, this will produce 1.0×10^{55} erg of energy at a rate of 1.0×10^{40} erg s $^{-1}$, which is comparable to the SN Ia heating rate of an entire galaxy (see Fig. 10). Thus, it could be that the gas in the very center of the

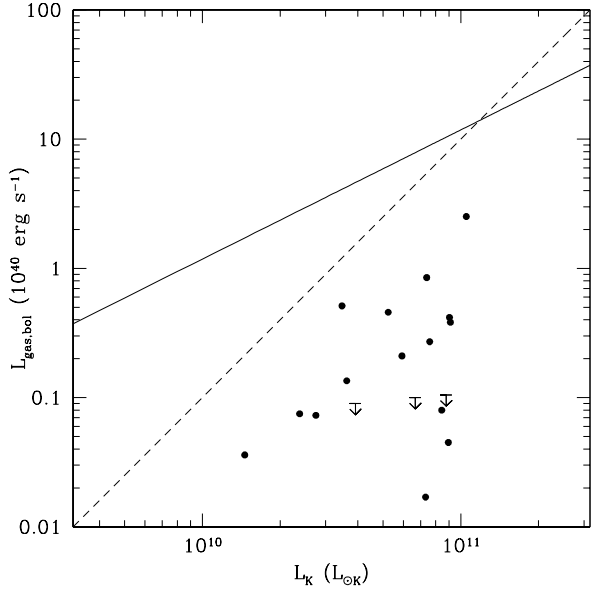


FIG. 11.— Scatter plot of the bolometric X-ray luminosity of the gas vs. the K-band luminosity of the galaxies. The inverted arrows are 90% upper limits. The solid line is the estimated SN Ia heating rate and the dashed line is the estimated mechanical AGN heating rate.

galaxies does not partake in the global SN Ia wind, but periodically accretes into the central black hole.

Environment can also play a significant role in the gas content of early-type galaxies. XMM-Newton and Chandra observations of early-type galaxies in the Coma cluster have shown that these galaxies can be either under luminous or over luminous in X-rays relative to field galaxies with comparable optical luminosities due to the competing effects of adiabatic compression, ram pressure stripping and thermal evaporation (Vikhlinin et al. 2001; Finoguenov & Miniati 2004; Hornschemeier et al. 2005). Due to the large distance of the Coma cluster, these observations were only sensitive to the X-ray properties of luminous early-type galaxies which have massive hydrostatic coronae in regions outside of dense groups or clusters. Low luminosity field galaxies, however, should have strong winds due to the lack of a confining ambient medium.

NGC4552 is located in the densest environment of any of the galaxies in our sample and clearly shows the effects of its environment. It is located $72'$ (a projected distance of 360 kpc) from the center of the Virgo cluster and has the highest gas content and hosts the most radio luminous AGN in our sample. The Chandra image shows that NGC 4552 has a leading cold front and a trailing wake of ram pressure stripped gas (Machacek et al. 2005). Based on the pressure jump across the cold front, Machacek et al. estimated that NGC4552 is traveling at 1600 km s^{-1} . The average gas density and pressure in NGC4552 derived from the values in Table 5 are $\langle n_e \rangle = 1.7 \times 10^{-3} \text{ cm}^{-3}$ and $\langle P \rangle = 1.9 \times 10^{-3} \text{ keV cm}^{-3}$. Using the results in Machacek et al., the ram pressure of the Virgo gas at the leading cold front in NGC4552 is $P_{ram} = 2.2 \times 10^{-3} \text{ keV cm}^{-3}$, which is greater than the average thermal pressure of the gas, but less than the central pressure of $P_0 = 3.5 \times 10^{-2} \text{ keV cm}^{-3}$. These calculations are in good agreement with the fact that some of the outer gas in NGC452 is being stripped as it falls into the Virgo cluster, but not the central gas. Based on the inferred velocity of NGC4552, it should have traveled approximately 2 Mpc during the time it has taken to accumulate its present gas mass. The ROSAT all-sky survey data show that the

gas in Virgo follows a $\beta = 0.47$ profile (Schindler et al 1999). Assuming the Virgo gas is isothermal and a radial trajectory for NGC4552, the thermal pressure of the Virgo gas surrounding NGC4552 would have increased by a factor of 20 during this time and the ram pressure by an even greater factor due to the increasing infall velocity. Thus, the ambient pressure during most of this time was sufficient to suppress the formation of a galactic wind, but insufficient to strip the gas from the galaxy. This would have led to a substantial increase in gas mass which could have triggered the AGN outburst.

10. SUMMARY

We have presented a systematic analysis of Chandra observations of 18 low-luminosity early-type galaxies. Emission from LMXBs is very significant in these galaxies and comprises between 30 to 95% of the total 0.5-2.0 keV emission. We find that the combined X-ray luminosity of LMXBs (resolved plus the power-law component of the unresolved emission) scales approximately linearly with L_K among the galaxies in our sample with an average $L_{X,LMXB}/L_K$ ratio comparable to that found in more luminous early-type galaxies. The gas temperature in these galaxies varies from 0.2 to 0.8 keV and roughly follows the observed trend between gas temperature and stellar velocity dispersion among more luminous early-type galaxies, albeit with significant scatter. The ratio of energy per unit mass in the galaxies to that in the gas, β_{spec} , varies from 0.3 to 1.0, indicating the presence of significant non-gravitational heating in most of the galaxies. We do not find any correlation between gas temperature and $L_{X,gas}$, unlike more luminous galaxies.

All of the galaxies in our sample are gas poor with $M_{gas}/M_* = 0.2 - 3.0 \times 10^{-3}$, compared to $M_{gas}/M_* = 0.01$ in more luminous early-type galaxies. The observed gas mass is much less than that expected from the accumulation of stellar mass loss over the lifetime of the galaxies. Based on recent estimates of the stellar mass loss rate in early-type galaxies, the time required to accumulate the observed gas mass is $10^8 - 10^9 \text{ yr}$. Due to the low gas densities, the cooling time of the gas is significantly longer than the replenishment time. Thus, most of the gas shed by evolving stars in these galaxies could not have condensed out of the hot phase and formed stars, and must have been expelled from the galaxies in a wind. The only exception to this is the most optically luminous galaxy in our sample, NGC4552.

Based on recent estimates of the SN Ia rate and mechanical AGN heating rate in early-type galaxies, we find that, on average, heating by type Ia supernova should dominate over AGN heating in galaxies with $L_K \lesssim 10^{11} L_{\odot K}$. Using the stellar mass loss rate in Athey et al. (2002) and the SN Ia rate in Cappellaro et al. (1999), we find that SN Ia are energetically capable of driving galactic winds in low-luminosity early-type galaxies even if the present SN Ia rate has been overestimated by a factor of two or the stellar mass loss rate has been underestimated by a factor of two. We also find that most of the supernova energy must be consumed in lifting the gas out of the gravitational potential well of the galaxies, with little energy converted into thermal or bulk kinetic energy of the gas.

If heating by SN Ia were the dominant heating mechanism at all times, it would be difficult to account for the large scatter in gas properties among the galaxies in our sample. Even though our calculations show that the time-averaged AGN heating rate is less than the supernova heating rate, the episodic nature of AGN outbursts could produce periods when AGN heating dom-

inates. One possible explanation for the large scatter in gas properties is that galaxies with very little gas at the present time recently experienced a significant AGN outburst that produced a rapid expulsion of the gas. Six of the galaxies in our sample were detected in the NVSS (Condon et al. 1998), however, we do not find any correlations between M_{gas}/M_* and radio power. The lack of a correlation may simply result from the time delay between when the AGN reaches its peak radio power and when the gas is expelled from the galaxy. In fact, the most ra-

dio luminous AGN in our sample has the largest gas mass. Another possible source for the observed scatter in gas properties among early-type galaxies is variations in the ambient gas pressure surrounding the galaxies which would impact their ability to develop galactic winds.

We would like to thank the referee, Mike Loewenstein, for his many useful comments. We also had many useful discussions of our work with Ewan O'Sullivan and Jan Vrtilek. This work was supported by NASA grant AR4-5016X.

REFERENCES

- Angelini, L. et al. 2001, *ApJ*, 557, L35.
 Athey, A., Bregman, J., Bregman, J., Temi, P. & Sauvage, M. 2002, *ApJ*, 571, 272.
 Bell, E. & de Jong, R. 2001, *ApJ*, 550, 212.
 Best, P., Kaiser, C., Heckman, T. & Kauffmann, G. 2006 (astro-ph 0602171).
 Birzan, L., Rafferty, D., McNamara, B., Wise, M. & Nulsen, P. 2004, *ApJ*, 607, 800.
 Blanton, E., Sarazin, C. & Irwin, J. 2001, *ApJ*, 552, 106.
 Blanton, E., Sarazin, C. & McNamara 2003, *ApJ*, 585, 227.
 Bower, R., Benson, A., Malbon, R., Helly, J., Frenk, C., Baugh, C., Cole, S. & Lacey, C. 2005, (astro-ph 0511338).
 Brighenti, F. & Mathews, W. 1999, *ApJ*, 512, 65.
 Cappellaro, E., Evans, R. & Turatto, M. 1999, *A&A*, 351, 459.
 Ciotti, L., De'Ercole, A., Pellegrini, S. & Renzini, A. 1991, *ApJ*, 376, 380.
 Colbert, E., Heckman, T., Ptak, A., Strickland, D. Weaver, K. 2004, *ApJ*, 602, 231.
 Condon, J. Cotton, W., Greisen, E., Yin, Q., Perley, R., Taylor, G. & Broderick, J. 1998, *AJ*, 115, 1693.
 Croton, D., Springel, V., White, S., DeLucia, G., Frenk, C., Gao, L., Jenkins, A., Kauffmann, G., Navarro, J. & Yoshida, N. 2006, *MNRAS*, 365, 11.
 David, L., Forman, W. & Jones, C. 1990, *ApJ*, 359, 29.
 David, L., Forman, W. & Jones, C. 1991, *ApJ*, 369, 121.
 de Vaucouleurs, G., de Vaucouleurs A., Corwin, H., Buta, R., Paturel, G. & Fouque, P. 1991, *Third Reference Catalog of Bright Galaxies* (Springer-Verlag:Berlin).
 Di Stefano, R. & Kong, A. 2004, *ApJ*, 609, 710.
 Faber, S. & Gallagher, J. 1976, *ApJ*, 204, 365,
 Faber, S. & Jackson, R. 1976, *ApJ*, 204, 668.
 Faber, S., Wegner, G., Burstein, D., Davis, R., Dressler, A., Lynden-Bell, D. & Terlevich, R. 1989, *ApJ Suppl*, 69, 763.
 Fabian, A., Sanders, J., Allen, S., Crawford, C., Iwasawa, K., Johnstone, R., Schmidt, W. & Taylor G. 2003, *MNRAS*, 344, 43.
 Finoguenov, A. & Jones, C. 2002, *ApJ*, 574, 754.
 Finoguenov, A. & Miniati, R. 2004, *A&A*, 418, L21.
 Forman, W., Jones, C. & Tucker, W. 1985, *ApJ*, 293, 102.
 Forman, W., Nulsen, P., Heinz, S., Owen, F., Eilek, J., Vikhlinin, A., Markevitch, M., Kraft, R., Churazov, E., Jones C. 2005, *ApJ*, 635, 894.
 Fukazawa, Y., Botoya-Nonesu, J., Pu, J., Ohto, A. & Kawano, N. 2006, *ApJ*, 636, 698.
 Gebhardt, K. et al. 2000, *ApJ*, 539, 13.
 Gilfanov, M. 2004, *MNRAS*, 349, 146.
 Grevesse, N. & Sauval, A.J. 1998, *Space Science Rev.*, 85, 161.
 Hornschemeier, A., Mobasher, B., Alexander, D., Bauer, F., Bautz, M., Hammer, D., Poggianti, B. 2005, (astro-ph 0512547).
 Humphrey, P., Buote, D., Gastaldello, F., Zappacosta, L., Bullock, J., Brighenti, F. & Mathews, W. 2006 (astro-ph 0601301).
 Irwin, J., Athey, E. & Bregman, J. 2003, 587, 356.
 Jarrett, T., Chester, T., Cutri, R., Schneider, S. & Huchra, J. 2003, *AJ*, 125, 525.
 Jones, C., Forman, W., Vikhlinin, A., Markevitch, M., David, L., Warmflash, A., Murray, S. & Nulsen, P. 2002, *ApJ*, 567, 115.
 Jones, C. et al. 2006, (in preparation).
 Jordan, A. et al. 2004, *ApJ*, 613, 279.
 Kahabka, P. & van den Heuvel, E. 1997, *ARA&A*, 35, 69.
 Kim, D., Fabbiano, P. & Trinchieri, G. 1992, *ApJ*, 393, 134.
 Kim, D. & Fabbiano, G. 2004, *ApJ*, 611, 846.
 Kraft, R., Kregenow, J., Forman, W., Jones, C., Murray, S. 2001, *ApJ*, 560, 675.
 Kraft, R., Viquez, S., Forman, W., Jones, C., Murray, S., Hardcastle, M., Worrall, D. & Churazov, E. 2003, 129, 146.
 Lauer, T. et al. 2005, *AJ*, 129, 2138.
 Loewenstein, M. & Mathews, W. 1987, *ApJ*, 319, 614.
 Machacek, M., Jones, C., Forman, W. & Nulsen, P. 2005 (astro-ph 0508588).
 Mathews, W. & Baker, J., 1971, *ApJ*, 170, 241.
 McLure, R. & Dunlop, J. 2002, *MNRAS*, 331, 705.
 McNamara, B. et al. 2000, *ApJ*, 534, 135.
 Navarro, J., Frenk, C. & White, S. 1996, *ApJ*, 462, 563.
 Nulsen, P., McNamara, B., Wise, M. & David, L. 2005a, *ApJ*, 628, 629.
 Nulsen, P., Hambrick, D., McNamara, B., Rafferty, D., Birzan, L., Wise, M., David, L. 2005b, *ApJ*, 625, 9.
 O'Sullivan, E., Forbes, D. & Ponman T. 2001, *MNRAS*, 328, 461.
 O'Sullivan, E., Ponman, T. & Collins, R. 2003, *MNRAS*, 340, 1375.
 Pellegrini, S. & Fabbiano, G. 1994, 429, 105.
 Pellegrini, S. 2005, *MNRAS*, 364, 169.
 Pence, W., Snowden, S., Mukai, K. & Kuntz, K. 2001, *ApJ*, 561, 189.
 Rosati, P. et al. 2002, *ApJ*, 566, 667.
 Sarazin, C., Irwin, J. & Bregman, J. 2000, *ApJ*, 544, L101.
 Sarazin, C., Irwin, J. & Bregman, J. 2001, *ApJ*, 556, 533.
 Sarazin, C., Kundu, A., Irwin, J., Sivakoff, G., Blanton, E., Randall, S. 2003, *ApJ*, 595, 743.
 Schindler, S., Binggeli, B. & Bohringer, H. 1999, *A & A*, 343, 420.
 Swartz, D., Ghosh, K., Suleimanov, V., Tennant, A. & Wu, K. 2002, *ApJ*, 574, 382.
 Tammann, G. 1982, in "Supernovae: A survey of current research; Proceedings of the Advanced Study Institute", (Cambridge: England), p. 371.
 Tonry, J. 2001, *ApJ*, 546, 681.
 Trinchieri, G. & Fabbiano, G. 1985, *ApJ*, 296, 447.
 Vikhlinin, A., Markevitch, M., Forman, W. & Jones, C. 2001, *ApJ*, 555, L87.
 Wargelin, B., Markevitch, M., Juda, M., Kharchenko, V., Edgar & Dalgarno, A. 2004, *ApJ*, 607, 596.
 White, S. & Frenk, C. 1991, *ApJ*, 379, 52.
 White, R., Sarazin, C. & Kulkarni, S. 2002, *ApJ*, 571, 23.
 Wilson, C., Patel, S., Kouveliotou, C., Jonker, P., Van der Klis, M., Lewin, W., Belloni, T. & Mendez, M. 2003, *ApJ*, 596, 1220.

APPENDIX

WIND SONIC POINT

Consider a steady, spherical wind driven by energy injected in association with stellar mass loss. Following Mathews & Baker (1971), we assume that stellar mass loss is distributed smoothly and mixes well with the hot ISM, so that we may treat the wind as a single, smooth fluid, with distributed mass injection. The equation of mass conservation is then

$$\frac{1}{r^2} \frac{d}{dr} \rho v r^2 = \alpha, \quad (1)$$

where r is the radius, ρ is the gas density, v is its radial velocity and $\alpha(r)$ is the mass injection rate per unit volume due to stellar mass loss. Assuming that the wind extends right to the center of the galaxy, this equation can be integrated to give the mass flow rate through a sphere of radius r ,

$$\dot{M}(r) = 4\pi\rho v r^2 = \int_0^r \alpha(r') 4\pi r'^2 dr' = \frac{4\pi}{3} \bar{\alpha} r^3, \quad (2)$$

where we have also defined $\bar{\alpha}(r)$, the mean stellar mass loss rate per unit volume within r . The momentum equation for the steady wind is

$$\rho v \frac{dv}{dr} = -\frac{dp}{dr} - \rho g - \alpha v, \quad (3)$$

where p is the gas pressure and $g(r)$ is the acceleration due to gravity (positive inward). The energy equation may be written

$$\frac{1}{r^2} \frac{d}{dr} \rho v r^2 (H + \frac{1}{2} v^2 + \phi) = \alpha(\varepsilon + \phi), \quad (4)$$

where H is the specific enthalpy,

$$H = \gamma p / [(\gamma - 1)\rho], \quad (5)$$

γ is the ratio of specific heats, ϕ is the gravitational potential and ε is the total energy per unit mass that is deposited in the flow along with the stellar mass loss. This is due principally to supernova heating, but includes kinetic energy due to random stellar motions, energy injected by planetary nebulae, etc. Following the usual practice, we assume that ε does not vary throughout the galaxy. Integrating the energy equation gives

$$\dot{M}(H + \frac{1}{2} v^2 + \phi) = \int_0^r \alpha(r') [\varepsilon + \phi(r')] 4\pi r'^2 dr' = \dot{M} w, \quad (6)$$

which also defines $w(r)$, a known function of the radius, and we have

$$w(r) = H + \frac{1}{2} v^2 + \phi. \quad (7)$$

We ignore the effects of radiative energy loss, which would clearly increase the energy required to drive the wind. These are generally small for the systems considered here.

From equation (2), the density can be given in terms of the velocity as

$$\rho = \frac{\bar{\alpha} r}{3v}, \quad (8)$$

and from equations (7) and (5) we get

$$\frac{p}{\rho} = \frac{\gamma - 1}{\gamma} (w - \frac{1}{2} v^2 - \phi). \quad (9)$$

These can be used to eliminate the pressure derivative from the momentum equation (3), giving, after some algebra,

$$\rho (v^2 - s^2) \frac{dv}{dr} = \frac{\bar{\alpha}}{3} \left[2(\gamma - 1)(w - \frac{1}{2} v^2 - \phi) - v_K^2 \right] - \alpha \left[\frac{\gamma + 1}{2} v^2 + (\gamma - 1)\varepsilon \right], \quad (10)$$

where the sound speed, s , is given by

$$s^2 = \gamma p / \rho \quad (11)$$

and the Kepler speed, v_K , is defined by $v_K^2(r) = gr$. Note that in order to obtain this result, we have used $g = d\phi/dr$ and differentiated the definitions of $\bar{\alpha}$ (equation 2) and w (equation 6).

The wind solutions starts with $v = 0$ at $r = 0$, passes through a sonic point, where $v = s$, and ends up as a freely expanding, supersonic flow for $r \rightarrow \infty$. At the sonic point $v^2 = s^2 = (\gamma - 1)(w - v^2/2 - \phi)$ (equations 9 and 11), so that

$$v^2(r_s) = \frac{2(\gamma - 1)}{\gamma + 1} [w(r_s) - \phi(r_s)], \quad (12)$$

where r_s is the radius of the sonic point. In order for the solution to pass through the sonic point, the right hand side of equation (10) must vanish there. After using equation (12) to eliminate the velocity, the resulting condition may be written

$$\left[\frac{4\bar{\alpha}(r_s)}{3(\gamma + 1)} - \alpha(r_s) \right] [w(r_s) - \phi(r_s)] = \alpha(r_s)\varepsilon + \frac{\bar{\alpha} v_K^2}{3(\gamma - 1)}. \quad (13)$$

The terms on the right of this equation are both positive and, since $H + v^2/2 > 0$, equation (7) requires $w - \phi > 0$ too. Thus

$$\frac{4\bar{\alpha}(r_s)}{3(\gamma+1)} > \alpha(r_s). \quad (14)$$

Defining

$$\bar{\phi}(r) = \frac{\int_0^r \alpha(r') \phi(r') r'^2 dr'}{\int_0^r \alpha(r') r'^2 dr'}, \quad (15)$$

from the definition of w (equation 6), we have $w(r) = \varepsilon + \bar{\phi}(r)$. Using this in equation (13) and solving for ε gives

$$\varepsilon \left[\frac{4\bar{\alpha}(r_s)}{3(\gamma+1)} - 2\alpha(r_s) \right] = \left[\frac{4\bar{\alpha}(r_s)}{3(\gamma+1)} - \alpha(r_s) \right] [\phi(r_s) - \bar{\phi}(r_s)] + \frac{\bar{\alpha}(r_s)}{3(\gamma-1)} v_K^2(r_s). \quad (16)$$

Since ϕ is an increasing function of the radius, $\phi(r_s) - \bar{\phi}(r_s) > 0$, and we showed that the factor multiplying it is positive above (14). Thus, we must also have

$$\frac{2\bar{\alpha}(r_s)}{3(\gamma+1)} > \alpha(r_s). \quad (17)$$

Under the usual assumption that α is proportional to the stellar density, this condition requires the mean density to be substantially greater than the local density at the sonic point. Thus, the sonic point must occur well outside the dense stellar core of a typical galaxy. We can now rewrite the result for ε as

$$\varepsilon = \left[\phi - \bar{\phi} + \frac{(\gamma+1)v_K^2}{4(\gamma-1)} + \alpha \left\{ \phi - \bar{\phi} + \frac{(\gamma+1)v_K^2}{2(\gamma-1)} \right\} \right]_{r=r_s} \left/ \left\{ \frac{4\bar{\alpha}}{3(\gamma+1)} - 2\alpha \right\} \right., \quad (18)$$

knowing that all of the factors in the term multiplied by α are positive. For a galaxy model with specified potential and stellar mass loss rate, α , this expression enables us to determine the specific energy injection rate, ε , from the location of the sonic point. Alternatively, if the energy injection rate is known, this equation may be solved to find the location of the sonic point. In particular, in the limit of large energy input, the sonic point approaches the radius that makes the denominator of the second term vanish, i.e., that makes the inequality (17) an identity.

For the remainder of this discussion, we assume that the stellar mass loss rate is proportional to the stellar density. Inside a galaxy, the right hand side of the expression for ε is generally a decreasing function of the sonic radius, r_s , so that the energy input required to drive a wind is minimized when the sonic point occurs at large r . If the stellar density falls rapidly to zero at the edge of the galaxy, α falls to zero quickly, while the other terms in this expression are continuous. Thus there is a rapid reduction in the energy required to drive the wind as the sonic point moves across the outer edge of the galaxy. As a result, the sonic point occurs close to the edge of the stellar distribution for a range of values of ε .

Beyond the edge of the stars $\alpha = 0$ so that $\bar{\phi}(r)$ is constant (from the definition 15). The remaining variable terms in (18), $\phi(r) + (\gamma+1)v_K^2(r)/[4(\gamma-1)]$, may increase or decrease with radius, depending on the value of γ and the distribution of the gravitating matter (which may extend beyond the stars). For $\gamma = 5/3$, these terms reduce to $\phi(r) + v_K^2(r)$, which is a non-decreasing function of r (since $v_K^2(r) = GM(r)/r$, where $M(r)$ is the gravitating mass within r), so that the global minimum of the expression (18) occurs at a value of r_s close to, or immediately outside the edge of the stellar distribution. However, the local condition for the sonic point (18) does not guarantee that the wind solution can be extended to infinity. Beyond the edge of the stars, $w(r)$ is also constant, and it is evident from equation (7) that it necessary that $w = \varepsilon + \bar{\phi} \geq 0$ for the wind solution to extend to $r = \infty$, an essential requirement for a steady wind. Thus the global minimum value of ε required for a wind when $\gamma = 5/3$ is

$$\varepsilon_{\min} = -\bar{\phi}(\infty). \quad (19)$$

Similar considerations apply for $\gamma < 5/3$, except that the energy requirement may now be minimized for $r_s \rightarrow \infty$ in equation (18). Thus we arrive at the same global value for ε_{\min} . Note that, for $\gamma = 5/3$, the wind solution with $w = 0$ attains a constant Mach number beyond the edge of the gravitating matter, rather than having the Mach number approach infinity. For $\gamma < 5/3$, when the energy requirement is minimized for $r_s \rightarrow \infty$, the flow would be subsonic everywhere. In that case, the effect of a disturbance at finite r is felt throughout the wind flow. In either case, the wind solution is fragile. This is not surprising for a wind driven with the absolute minimum energy. It emphasizes that the minimum energy requirement is just that. In reality, greater energy is required to sustain a wind.

To evaluate $\bar{\phi}$, we assume that the gravitational potential has the NFW form,

$$\phi(r) = -4\pi G\rho_0 a^2 \left[\frac{\ln(1+r/a)}{r/a} - \frac{1}{1+c} \right], \quad \text{for } r < ac, \quad (20)$$

where a is the scale length, ρ_0 is the scale density and c is the concentration parameter. The stars, hence the mass injection rate, are assumed to have the King model distribution

$$\alpha(r) = \frac{\alpha_0}{(1+r^2/b^2)^{3/2}}, \quad (21)$$

where b is the core radius. Using the definition (15), we then get

$$\bar{\phi}(r) = -4\pi G\rho_0 a^2 \left[-\frac{1}{1+c} + \frac{1}{\ln(y + \sqrt{1+y^2}) - y/\sqrt{1+y^2}} \right]$$

$$\times \left\{ -\frac{\ln(1+\beta y)}{\beta\sqrt{1+y^2}} + \frac{1}{\sqrt{1+\beta^2}} \ln \frac{(1+\beta y + \beta\sqrt{1+y^2} - \sqrt{1+\beta^2})(1+\beta + \sqrt{1+\beta^2})}{(1+\beta y + \beta\sqrt{1+y^2} + \sqrt{1+\beta^2})(1+\beta - \sqrt{1+\beta^2})} \right\}, \quad (22)$$

(23)

where $\beta = b/a$, $y = r_c/b$ and the stellar distribution is cut off at r_c . The normalizing factor for the NFW potential, $4\pi G\rho_0 a^2$, was determined from the assumption that the maximum rotation speed is related to the line-of-sight velocity dispersion by $v_{K,\max}^2 = 2\sigma^2$, giving

$$4\pi G\rho_0 a^2 = \lambda\sigma^2, \quad (24)$$

with $\lambda \simeq 9.25$. Equating the mean density of the halo to χ times the critical density then gives the scale length,

$$a = \frac{\sigma}{H_0} \sqrt{\frac{2\lambda [\ln(1+c) - c/(1+c)]}{\chi c^3}}, \quad (25)$$

where H_0 is the Hubble constant. Parameters for the King model are set to match photometric properties of the galaxies.